JOINT EUROPEAN TORUS

JET–P(89)06

M. Mattioli, N.J. Peacock, H.P. Summers, B. Denne, N.C. Hawkes
and JET Team

Contributions from Ion-Atom Charge Exchange Collisions to the CVI Lyman Intensities in the JET Tokamak

Contributions from Ion-Atom Charge Exchange Collisions to the CVI Lyman Intensities in the JET Tokamak

M. Mattioli[1], N.J. Peacock[2], H.P. Summers[3], B. Denne[3], N.C. Hawkes[2]
and JET Team*

JET-Joint Undertaking, Culham Science Centre, OX14 3DB, Abingdon, UK

[1]Association Euratom-CEA sur la Fusion, CEN Cadarache, F-13118 St Paul Lez Durance, France
[2]The Culham Laboratory (Euratom-UKAEA Fusion Association), Abingdon, Oxon OX14 3DB, UK
[3]JET Joint Undertaking, Abingdon, Oxon OX14 3EA, UK
** See Appendix 1*

Preprint of Paper to be submitted for publication in
Journal de Physique Colloques

ABSTRACT.

In a multi-keV temperature deuterium plasma such as JET, CVI emission arises from collision processes which, in the absence of neutral deuterium beam heating, occur near the plasma boundary. Distortions to the CVI Lyman decrement. such as the Ly $\beta/\gamma/\delta$ ratio and enhancement of the high quantum states (n~12) are observed. These are correlated to the D_α intensity and consequently to the influx of D° atoms at the plasma boundary. The intensities of the Lyman spectra are interpreted in terms of low energy electron transfer from thermal D^o atoms to C^{+6} ions as well as electronic excitation of 6^{+5} ions in their ground state. The line-of-sight emission is modelled using an impurity ion transport code with input data on the electron and D^o profiles. Electron transfer from excited states of D^o (up to the thermal limit) as well as the ground state have to be included to give satisfactory agreement with the CVI Lyman spectra when the D^o influx is high. The cross-sections for charge-transfer from excited states have been estimated using a simple Landau-Zener model. Comparison of the relative intensities of the CVI Lyman series Ly $\beta/\gamma/\delta$ etc with the model calculations allows plausible corrections to be made to the effective charge transfer cross-section as a function of principle quantum number. The observations offer a potential method of measuring local D^o concentrations near the boundary of high temperature, high D^o recycling plasmas, but limited at present by the uncertainties of low energy charge transfer cross-sections.

1. INTRODUCTION

The influence of charge-exchange processes (CX) between impurity ions and neutral hydrogen isotopes has been reported in the observed line spectra from Tokamak plasmas. These neutrals can be either thermal neutrals or beam neutrals. The atomic beams are used for heating or diagnostic purposes (or both) with energies in the tens of keV range. Background thermal neutrals are present in Tokamak plasmas from the periphery to the centre as a consequence of inward transport due to successive charge-exchange collisions with plasma ions. Their concentration is several order of magnitude larger at the edge than at the centre and several orders of magnitude lower everywhere than the electron density. Also secondary "halo" (produced by successive beam-ion collisions) can add a substantial concentration of thermal neutrals at the centre with atomic beam heating. Such charge-exchange collisions also yield a supplementary recombination process for impurity ions, and so influence impurity ionization equilibrium and impurity transport evaluations. The electrons "exchanged" between the hydrogen isotope neutrals and the impurity ions are predominantly captured into excited states of the recombined ions and so can be detected by observation of the cascade radiation emitted during decay to the ground state. From the decay spectral series, quantitative estimates of the ionic concentrations can be made, provided the effective CX rates (including cascades and level mixing) are reliable and the atomic densities and electron parameters in the plasma are known.

Generally, this allows detection of the fully-stripped carbon and oxygen ions, not normally observable by line emission spectroscopy. Moreover, the impurity ion temperature and toroidal rotation can be obtained by linewidth and lineshift evaluations. These techniques, called charge-exchange recombination spectroscopy, have been reviewed recently by Isler [1]. In JET, measurements of the impurity ion density, temperature and rotation have been performed by observing visible transitions between highly excited levels of the recombined C and O H-like ions with the supplementary heating beams active [2].

Space-resolved spectra of the $1s^2$-1snp Ar XVII singlet lines have been observed on Alcator-C [3,4]. In these latter papers, in ohmic plasmas without atomic beams the line intensity ratios could not be simulated by radiative cascades of the upper levels populated by electron collisions from the ground state, but charge-exchange collisions with thermal neutrals (either in their ground states or in their excited states) had to be added as a supplementary process populating the highly excited states. From a numerical simulation of the space-resolved spectra it was possible to obtain the neutral hydrogen radial density profile.

In this paper we shall present experimental carbon Lyman series spectra obtained in ohmically- and radiofrequency-heated JET plasmas. The UV spectrometers view the carbon inner-wall directly along a horizontal chord. The outer belt limiters, being displaced from the horizontal, are not seen in this viewing geometry. When the plasma is brought into contact with the inner-wall [the so-called inner-wall (IW) plasmas to be distinguished from the limiter (L) plasmas, in which the plasma current channel is limited by the outer belt limiters] modifications to the emission of the series extend to the series limit. The experimental C spectra then resemble both the previously mentioned Ar spectra [3,4] and the spectra predicted in [5] for the C and O Lyman series in the presence of high energy neutral beams.

In Section 2, after a short description of the experimental set-up, we shall present data from a 3.5 MA, 2.8 T JET discharge, which, having been initially started as an L discharge, is moved to the inner-wall at about 5 sec after the beginning of the pulse. It is subsequently heated, between 11.5 sec and 15 sec, by 3 MW of radiofrequency (RF) power.

In Section 3 the impurity transport simulation code is described with particular attention to the atomic physics data, and then in Section 4 the carbon Lyman spectra during three selected time intervals (corresponding to the three distinct experimental phases of the discharge) are

simulated. In the simulations, the thermal deuterium neutral density $n_D(r)$ radial profile is treated as a free adjustable parameter. To model all three experimental situations with "reasonable" $n_D(r)$ profiles (i.e. not in contradiction to other diagnostics) it will be shown to be necessary to introduce corrective, principal quantum number (n)-dependent, multiplicative factors F(n) into the effective CX rate coefficients for photon emission in the Lyman series.

In the concluding Section 5, the possibility of measuring local D° concentrations near the boundary of high temperature, high D° recycling plasmas is discussed.

2. EXPERIMENTAL

2.1 General

The 10-330 A° region is observed in JET (Joint European Torus) by using the most recent version of the Schwob-Fraenkel 2m grazing incidence XUV spectrometer [6]. It is located in the torus midplane and views the plasma along a central chord at a slight angle to the major radius of the JET torus. The spectral resolution (with a 600 grooves/mm grating) is 0.2 Å (FWHM). The detector consists of two microchannelplate (MCP) detectors movable along the Rowland circle. Each is associated with a phosphor screen image intensifier and coupled by a flexible fibre optic conduit to a 1024 element photodiode array. In the present experiment, one detector is positioned to view the C VI Lyman series, whereas the other includes in its spectral range the C VI 182.17 Å Balmer α line. Longer wavelength lowly-ionised carbon lines (eg. C III 977 Å and C IV 312.4 Å) are simultaneously observed with a McPherson VUV broad band survey spectrometer [7]. Absolute calibration is available only for the second spectrometer. Radial profiles of electron temperature, $T_e(r)$, electron density, $n_e(r)$, required for the simulation of the spectroscopic data, are obtained, respectively, from a Lidar Thomson scattering system [8] and from a FIR laser interferometer [9] (in this case Abel inversion taking into account the shape of the magnetic surfaces is required).

2.2 Discharges with large variations in the atomic deuterium influxes

In the following, a representative discharge showing changes in the C VI Lyman series intensities is analyzed. The discharge chosen (# 13571) is one of a series of deuterium discharges with plasma current I_p = 3.5 MA, toroidal magnetic field B_T = 2.8 T, ^{3}He prefilling and a few percent of H addition for ion-cyclotron RF minority heating.

Time-resolved signals showing the discharge evolution are presented in Figure 1 as follows : the average line integrated electron density $\overline{n_e}(t)$, the maximum central electron temperature $T_e(o,t)$ from electron cyclotron emission, the RF power, the horizontal distance Δ_H between the plasma and the inner-wall and two D_α monitors. The upper D_α signal in Figure 1, $D_{\alpha h}$, views horizontally both the plasma column and the inner-wall, while the lower, $D_{\alpha v}$, observes the plasma vertically far from limiters and RF antennae).

The discharge starts as an L discharge (Δ_H ~ 12 cm and low $D_{\alpha h}$ signal). After 5 sec the plasma is moved towards the inner-wall (Δ_H ~ 0, with concomitant large $D_{\alpha h}$ signals and with $D_{\alpha v}$ signals practically unchanged). After an almost steady state phase lasting until ~ 11.5 sec, 3 MW of RF power are applied between 11.5 and 15 sec during which there are increased values of both n_e and T_e. The discharge remains on the inner-wall throughout the additional heating. In the upper insets of Figure 1 a schematic of the two plasma configurations is given, showing the last closed surface in contact either with the inner-wall (right, IW plasma) or with the belt limiters (left, L plasma). The lines of sight of both the XUV spectrometer and the VUV spectrometer are also shown.

In Figure 2 the time evolutions of a number of relevent spectroscopic signals are shown (namely, C VI Lyman α, β and γ, C VI Balmer α, the C V resonance (R) and intercombination (I) lines, as well as C IV 312.4 Å and C III 977 Å lines). All the line brightnesses increase during the RF heating period (the same being true for the two D_α signals presented in Figure 1). By contrast, at the L-IW movement the brightness-time evolutions depend on the individual lines. C VI Lyα and Lyβ along with

C V R are not much affected by the plasma displacement, whereas all the other brightnesses show some degree of discontinuity : by as much as ~ 30 % for C V I, ~ 40 % for C VI Lyγ, ~ 100 % for C VI Balmer α and by one order of magnitude or more for the two lowly-ionized C lines. With IW plasmas, since the carbon sources are viewed directly (see Figure 1 inset), the C III and C IV brightnesses represent the local carbon influx rather than the influx averaged over the entire plasma surface [10].

2.3 C VI Lyman series spectra

The multichannel spectrometer records the entire C VI Lyman spectrum. Three spectra showing the region from Lyβ up to the series limit are presented in Figures 3 to 5 (upper), corresponding to the three phases of interest in the discharge. The corresponding time intervals are shown hatched in Figure 2. In contrast to the spectrum of the L plasma in Figure 3, in which the intensities of successive Lyman lines decrease monotonically with increasing quantum number n of the upper level, the spectra presented in Figures 4 and 5 show reduced Lyβ/Lyγ and Lyβ/Lyδ ratios and enhanced emission up to the series limit. Due to the 0.2 Å FWHM resolution, lines above Lyε are not resolved individually. This enhanced emission manifests itself as a "bump", the peak of which corresponds to about the 1s-12p member. It should be noted that similar modifications of line intensity ratios have been seen also in the $1s^2$-1snp singlet He-like C ion spectra [11,12]. For IW plasmas, enhancement of the C V series emission (albeit without the "bump") was observed up to the series limit. The He-like ion spectra will not be analyzed quantitatively in this paper, since the available CX cross section data leading to recombined He-like ions are not as well known as those leading to recombined H-like ions.

The spectra shown in Figures 3 to 5 (upper) give the detected signals (count number) as function of the wavelength (pixel number). The experimental count numbers have been corrected for pixel gain fatigue. The problem was first recognised on displacing the detector carriage around the Rowland circle, when "holes" appear in the background signal level at the pixels corresponding to the previous positions of the strongest lines. Pixel to pixel gain variations can arise due to differential ageing of the MCP [13]. The raw count numbers have been corrected by measuring the response to a continuum source provided by the plasma itself during a cold disruptive phase. The effect of these corrections is to increase the strong lines with respect to the weaker ones. They are most serious for the most intense lines such as Lyα.

The pixel "gain-sag" correction must also be applied to the C VI Lyα/Lyβ and to the C V I/R ratios. These lines are not shown in the spectra of Figures 3 to 5, but their ratios can be deduced from the brightness curves shown in Figure 2. Since the stronger C V R (resonance) line is more "affected" than the weaker C V I (intercombination) line, the I/R ratio is found to be reduced by a factor of 1.10-1.15. The Lyα/Lyβ ratio, see Figure 2, has to be corrected by up to a factor of two, i.e. to a value of about 10 from a raw uncorrected value of 5. Accurate values of the Lyα/Lyβ ratio are found in discharges in which the detector has been moved so that both lines are displaced to a previously line free set of pixels [11,12].

3. IMPURITY TRANSPORT SIMULATION CODE

3.1 Description of the code

Impurity transport in tokamak plasmas is studied by solving for each atomic species the following impurity transport system in cylindrical geometry

$$\frac{\partial n_Z}{\partial t} = -\frac{1}{r}\left(\frac{\partial}{\partial r}(r\Gamma_Z)\right) + n_e[n_{Z-1}\,S_{Z-1} - n_Z S_Z + n_{Z+1}\,\alpha^R_{Z+1} - n_Z\,\alpha^R_Z]$$

$$+ n_D[n_{Z+1}\,\alpha^{CX}_{Z+1} - n_Z\,\alpha^{CX}_Z] - \frac{n_Z}{\tau_p} \qquad Z = 1,\ldots,Z_N \tag{1}$$

where Γ_Z is the radial particle flux density (positive when directed outwards) of the ions of charge Z of an element of nuclear charge Z_N. n_Z is the corresponding ion density. S_Z, α^R_Z and α^{CX}_Z are, respectively, for the ions of charge Z the ionisation rate coefficients, the radiative plus dielectronic recombination rate coefficients and the CX recombination rate coefficients. τ_p (different from infinity only in the "scrape-off layer" (SOL)) is the impurity confinement time for particle transport along the field lines.

Input parameters of the code are the $n_e(r)$ and $T_e(r)$ profiles along with the thermal neutral deuterium radial profile $n_D(r)$. S_Z, α^R_Z and α^{CX}_Z are functions of the radius r because of their electron temperature dependance. In the evaluation of α^{CX}_Z it is supposed that both the recombining C ions and the D^+ ions have the same temperature T_i as the neutral deuterium atoms and that this temperature can be taken equal to T_e, at least in the external plasma region. Note that deuterium is the JET filling gas.

A separate equation has to be included to describe the ionization of neutral carbon of density n_o. The boundary condition at the last mesh radius r = a is written as

$$\Gamma_o(a) = n_o(a)\,V_o = R\,\Sigma_Z\,\Gamma_Z(a) + \Gamma_{ext} \tag{2}$$

that is $\Gamma_o(a)$, the total neutral carbon flux density entering into the plasma with directed velocity V_o, is set equal to the sum of an external flux density Γ_{ext} and a recycling flux density. The latter is the total outward flux density $\Sigma_Z\,\Gamma_Z(a)$ at the last mesh recycled with recycling coefficient R. The radial flux density Γ_Z is described by the following expression

$$\Gamma_Z = - D_A \frac{\partial n_Z}{\partial r} - \frac{r}{a} V_A n_Z \qquad (3)$$

where D_A (diffusion coefficient) and V_A (inward convection velocity) are two transport parameters independent of Z and of r.

The numerical solution of system (1) is the same as used previously for TFR plasma simulations [14] and is based on the procedure described in [15].

3.2 Atomic physics data

The atomic subroutines on ionisation balance are regularly updated to include the most recent theoretical collision data. For carbon ions, in the present version of the code, the ionisation rate coefficients S_Z are taken from the Queen's University of Belfast assessments [16] (updated in [17] for Li-like ions). The recombination rate coefficients α_Z^R are obtained as described in [18], whilst the total charge-exchange recombination rate coefficients α_Z^{CX} are taken from the recent ORNL assessments [19].

Line brightnesses and emissivities are also predicted. In order of increasing ion charge the atomic data used for the lines considered in the paper are the following : the two lowly-ionized ion lines C III 977 Å and C IV 312.4 Å have been calculated in the coronal population approximation (ie. electron excitation from the ground state followed by radiative decay) using excitation rate coefficients from [20] and [21], respectively. For Be-like ions $2s2p\ ^3P$ metastable population has to be considered. A singlet $2s^2\ ^1S_o$ ground state fractional population equal to 0.35 has been adopted following [22].

The two He-like ion lines (C V R and I) have been evaluated in the first instance in the coronal population approximation. It has to be borne in mind that the $1s2s\ ^{1,3}S$ populations are mixed by electron collisions with the $1s2p\ ^{1,3}P$ populations so enabling radiative decay to the ground state. The rate coefficients have been taken from [22,23], but ex-

trapolated toward large T_e-values following [19]. The ratio of the two lines is called the G-ratio and it is well known by astrophysicists to be a decreasing function of the electron temperature but only weakly dependent on the electron density [see [24] and references therein]. Corrections due to cascades from higher levels, which increase mainly the I line intensity and so the G-ratio, should be included. The upper levels can be populated either by electron excitation from the ground state or by recombination. The correction due to electron excitation can be estimated from [24], when cascading is included or excluded. Radiative and dielectronic recombinations of the H-like ions can be evaluated following [25]. CX contributions are included in the code by supposing that three quarters of the recombining collisions (ie. 0.75 α^{CX} for C^{5+} recombination) populate excited triplet states and that deexcitation to the ground state is only possible through the I line. This is a relatively crude approximation. Moreover, inner-shell ionisation of Li-like ions is a supplementary process producing excited He-like ions as described in [25].

3.3 Line emission from H-like carbon ions

To simulate H-like C ion emission a more sophisticated model has been adopted, since not only electron excitation from the ground state and CX collisions with deuterium atoms (both in ground and excited states) contribute, but redistribution and cascades modify their effects. The emission is modelled in a nlj subshell resolved calculation including principal quantum shells n up to 20 [2,26]. The model gives effective excitation rate coefficients for photon emission in all the Lyman and Balmer series lines decomposed into electon impact parts Q^E_{n-1}, Q^E_{n-2}, and CX parts Q^{CX}_{n-1}, Q^{CX}_{n-2}. It is to be noted that the corresponding contributions to the emissivities are, respectively, proportional to $n_e n_{C^{5+}}$ and to $n_D n_{C^{6+}}$. Local electron, ion and neutral deuterium temperatures and densities are used consistent with the ionization stage transport model.

An extension of the original model for the CX effecive rates was required to allow proper treatment of high series members. Charge transfer from thermal neutrals in the 1s state to form excited states of C^{5+} is strongly selective into principal quantum shell $n_{crit}(1s)$ of the receiving ion with very small contributions to levels $n > n_{crit}(1s)$. The 1s in brackets describes the state of the deuterium atoms. $n_{crit}(1s)$ (~ 4 for C) is the level for which the CX cross section is a maximum. The cross-sections for electron transfer from excited principal quantum shells n_h of deuterium scale approximately as n_h^4, while the associated $n_{crit}(n_h)$ scales as $n_h n_{crit}(1s)$. Excited states of the donor atom are therefore the principal source for populating the very high n shells of the C^{5+} ions. Relevant excited deuterium levels are restricted to $n_h \leq 5$ (the collision limit). The collision limit for C^{5+} is ≥ 20 in the present conditions and it does not influence the calculations. A collisional-radiative model has been used in the "bundle-n" picture [26] to calculate the excited level population of deuterium up to the collision limit.

Low energy, n-shell selective, charge transfer cross-sections from D(1s) have been taken from close-coupling molecular orbital (CCMO) calculations [27]. There are little data available for capture cross-sections from excited states of thermal neutrals. As a basis for comparison with experiments, we have adopted the Landau-Zener (LZ) approximation based on the generalized H_{12}^* coupling matrix element from [28]. An over-barrier model [29] gives larger values (by factors ~ 4-5) and with higher $n_{crit}(n_h)$. The expectation [28] is that the true values should lie between these two approximations. It is assumed that the capture is strongly selective into the appropriate n_{crit} and the l distribution is as for capture from ground state neutrals. The latter is not critical for calculating the l-state redistribution.

The solid curves in Figure 6 show as a function of the quantum number n the theoretical effective electron impact and charge-exchange rate coefficients (Q^E_{n-1} and Q^{CX}_{n-1}) for the Lyman series. The plasma parameters T_e ~ 500 eV, $T_i = T_e = T_D$, n_e ~ 1.4 10^{13} cm^{-3}, Z_{eff} ~ 2, chosen for

these calculations approximate to those which obtain in the region of dominant C VI emission. The detailed confrontation of experiment and theory to be described in Section 4 indicates that the Q^{CX}_{n-1} rates, especially those associated with capture from neutral excited states, should be increased, by multiplying them by a n-dependent factor F(n) (x 1,5 for n = 4,5, x 2,5 for n = 6-9, and x 4 for n = 10-15). The "corrected" Q^{CX}_{n-1} are shown by the dashed line and will be discussed further in the conclusions.

4. NUMERICAL SIMULATIONS OF THE CARBON LYMAN SERIES SPECTRA

4.1 General considerations

The $n_e(r)$ and $T_e(r)$ profiles required for the analysis are obtained by symmetrizing about the center of the last closed magnetic surface the full profiles across the whole plasma diameter (on the horizontal plane along the torus major radius). In this way both the inward displacement and the increased plasma dimension of the IW plasmas may be incorporated. The profiles are extrapolated up to the last mesh radius a. This is set a few centimeters beyond the radius a_L of the last closed magnetic surface. E-folding lengths comparable to those given by Langmuir probes in similar plasma conditions are adopted in the extrapolation. For the three plasma conditions simulated by the code, Table 1 gives the values of T_e and n_e at the centre, at the radius a_c of maximum simulated C VI line emissivity and at the limiter radius a_L. The deuterium neutral density profile $n_D(r)$ has been treated in the code as an adjustable parameter which can be varied to match the simulated and experimental spectra. From the three neutral particle analysers (NPA) [30] it is possible to obtain the maximum deuterium ion temperatures along the lines of sight. The D° concentration profiles are inferred [30] from an analysis of the energy spectra of the emitted neutral particles from JET during similar discharges. Note that the analysed particles come from a radial extent up to ~ 1/2-2/3 a_L and that the deduced profiles are globally consistent with NPA measured fluxes. However the numerical values, especially at larger radii up to the limiter radius a_L, have to be considered as tentative, since these are based only on a numerical neutral particle transport code.

We use as our starting point for $n_D(r)$ for L plasmas and for IW plasmas (both ohmic and RF-heated) the two solid line curves of Figure 7. The L plasma curve (a, curve 1) is a lower limit from NPA simulations of JET limiter plasmas, whereas for IW plasmas the reference curve (b, curve 3) is quite near to the curve given by NPA simulations of similar IW ohmic plasma conditions. The dashed curves are obtained by keeping constant n_D-values in the central region and increasing or decreasing n_D-values in the peripheral plasma with respect to the reference curves.

Numerically the two transport parameters (see formule 3) are taken as $D_A = 10^4$ cm^2/sec and $V_A = 200$ cm/s. The effect of varying them (within ranges believed typical for JET [31,32]) will be discussed in subsection 4.4.

Other parameters required for the simulations are the impurity confinement time τ_p in the SOL (between a and a_L), the recycling coefficient R, the velocity V_o and the external flux density Γ_{ext} of the incoming C atoms. Numerically, we choose $\tau_p = 10$ msec, $R = 0$, $V_o = 4\ 10^5$ cm/s. A steady state solution for constant Γ_{ext} of arbitrary magnitude is sought, which could then be normalised by comparison with absolute line brightnesses.

4.2 Radial ion distribution

The ion density radial profiles for IW plasmas are shown in Figure 8 (upper) for three n_D profiles, (a) without neutrals, and with (b) and (c) which correspond to neutral density profiles (2) and (3) of Figure 7b, respectively. In the same Figure 8 (lower), the emissivities of representative lines of C III, C IV, C V and C VI are shown. The figure caption indicates the scale factors by which both the ion densities, normalized to the central total ion density, and the line emissivities, normalized to the C III 977Å maximum emissivity for case (a) have been multiplied.

It appears that varying the $n_D(r)$ curve, while keeping other parameters constant, has a large effect on the line radiances. For example, between the two limiting situations shown in Figure 8, the C VI Lyβ, C V R, C IV 312.4 Å and C III 977 Å brightnesses vary, respectively, by

factors of 4.3, 6.7, 31 and 7. This fact is associated with the much slower effective ionisation of carbon ions when CX processes are present. It is apparent in Figure 8 since, progressing from (a) to (c), the C^{3+} to C^{5+} ion densities increase and the emissivity shells are displaced inwards. The brightness increase is an important point which will be considered further in Subsection 4.6. It will be proved that n_D increases significantly after moving to IW, and then a contradiction appears between the brightness dependence on n_D and the fact that (see Figure 2) C VI Lyα and Lyβ and C V R are practically constant at the L-IW shift.

4.3 Preliminary simulations of Lyman spectra

Once the steady state solution of equations (1) is attained, a subroutine plots the simulated Lyman spectra from the calculated brightnesses assuming a Gaussian instrumental function of 0.2 Å FWHM. Examples of simulated spectra are shown in Figure 9. The line brightnesses per unit wavelength are plotted in arbitrary units, as a function of the wavelength λ (in Å) from Lyβ up to the 1s-15p line. The instrumental resolution allows the distinct lines to be obtained up to Lyε, whereas individual higher n lines are not resolved. The "apparent" emission reaching the series limit at 25.3 Å.

For the case of IW plasmas and neutral density profile (3) of Figure 7b, Table 2 gives the multiplicative factors F(n) applicable to the theoretical effective CX rate coefficients Q^{CX}_{n-1} used for the four simulations displayed in Figure 9. In spectrum (a) (all F(n)-values are equal to one), unresolved line emission towards the series limit appears, but the chosen Q^{CX}_{n-1} rates are insufficient to reproduce the experimentally observed bump at about 25.5 Å, see Figures 4 and 5 (upper). Since curve (3) can be considered a reasonable initial guess for $n_D(r)$, we have to increase Q^{CX}_{n-1} for large n. On choosing F(n) = 2.5 for n in the range 6 to 9 and F(n) = 4 for n in the range 10 to 15, the spectrum (b) reproducing the experimental bump is generated. Simulations of the RF-heated phase (IW + RF) were unable to reproduce the experimental values of the Lyβ/Lyγ and Lyβ/Lyδ ratios (1.35 and 4.2, respectively) with F(4,5) = 1 even if curve (5) of Figure 7b is used for $n_D(r)$. This curve is considered an upper limit, since larger n_D-values have never been inferred in JET either

from NPA data analysis or from D_α monitors. Spectrum (c) shows decreased Lyβ/Lyγ and Lyβ/Lyδ ratios obtained by taking F(4,5) = 1.5. Finally, spectrum (d) shows the sensitivity of the simulated spectra to a further increase of F(n).

4.4 Influence of the impurity transport parameters

By reducing both D_A and V_A by a factor of two, it has been found that the simulated spectra are practically unaffected. Physically this can be explained by the fact that the Lyman line emitting shells are slightly displaced outwards, i.e. towards lower T_e-values. This should slightly increase the line ratios (i.e. increase the Lyman decrement), as a consequence of the exponential dependence on the temperature of the rates Q^E_{n-1}. Simultaneously, the influence of CX increases since emission takes place at larger n_D-values (although at slightly lower Q^{CX}_{n-1} rates, which are an increasing function of the temperature). The overall effect is that the emission spectra are essentially unaffected by a variation of both transport parameters together by up to a factor of two. Note that this implies no change in the total carbon ion radial density profiles, since the peaking is determined by the V_A/D_A ratio. Similarly, increasing the V_A/D_A ratio by a factor of two has no effect on the simulated spectrum.

Since these variations of the transport parameters can be considered typical for JET Ohmic and RF-heated plasmas [31,32], it is concluded that D_A and V_A are not sensitive factors as far as the Lyman spectrum is concerned.

4.5 Final simulations of the experimentally observed Lyman spectra

In subsection 4.3 it was shown that a multiplicative factor F(n) > 1 was necessary to simulate the reduced Lyβ/Lyγ and Lyβ/Lyδ ratios and the large-n "bump" associated with inner-wall plasmas. Clearly, the estimated $n_D(r)$ curve is affected by the F(n) values (the larger F(n) the smaller the inferred deuterium densities).

Fortunately another constraint can be obtained from the quanti-

tative analysis of the D_α monitor signals during the L phase. Simple considerations from the absolute brightnesses shown in Figure 1 (e) and (f), give peripheral n_D-values of a few 10^9 cm^{-3}. The excited state populations are taken from [33]. The assumption of poloidal symmetry of $D_\alpha$emission is justified by the similar brightnesses on the two D_α monitors observing the plasma vertically and horizontally. A SOL thickness of ~ 5 cm is assumed with comparable atomic and molecular neutral particle production at the boundary. Since no large-n "bump" and high Lyβ/Lyγ ratios appear on the corresponding spectra (see Figure 3 (upper)), the F(n) multiplicative factors must not be so large that they produce such a bump nor give too low Lyβ/Lyγ ratios when $n_D(a)$ is of the order of 1.5-3 10^9 cm^{-3}. Incidentally, the low-n F(n) multiplicative factors must not be increased by greater than a factor of two at most to remain consistent with the total CX rate for C^{6+}, α^{CX}, which is believed to be reliable.

In a similar manner to the case of IW plasmas presented in Figure 9, a series of four simulated spectra is presented in Figure 10, to show the effect of both F(n) and $n_D(r)$ variations for L plasmas. The adopted F(n)-values and $n_D(r)$ curves (from Figure 7a) are given in Table 3. The first three spectra show that, on increasing $n_D(r)$, the Lyβ/Lyγ and Lyβ/Lyδ ratios are reduced and that the large-n bump appears progressively. It is clearly present in spectrum (c). The fourth spectrum (d) shows, in comparison with spectrum (b), the effect of an increase of F(n). It indicates the sensitivity of the procedure used in the comparison of experimental and simulated spectra.

Table 4 shows the experimental and simulated Lyβ/Lyγ and Lyβ/Lyδ ratios for the three separate phases of the discharges. Column "C" indicates the n_D curve number from Figure 7 (a) for L plasmas, (b) for both IW plasmas, whereas the F(n)-values are those for spectra (c) in Tables 2 and 3. The final quantitative comparison is based on the Lyβ/Lyγ ratio (rather than on the much less varying and less sensitive Lyβ/Lyδ ratio) and on the shape of the simulated spectrum towards the series limit.

For L plasmas (the experimental spectrum between 2.5 and 4.2 sec is given in Figure 3 (upper)) the best correspondence lies between curves

(2) and (3) in figure 7a, ie. suggesting a peripheral n_D density of about 2 10^9 cm^{-3}. This is very close to the estimated value from D_α emission. We have verified this in a final check using the intermediate curve n_D shown in Figure 7a dotted. Table 4 shows that for IW plasmas (the experimental spectra between 7.7 and 10 sec and between 13.2 and 14 sec are given in Figures 4 and 5 (upper) for ohmic and RF-heated plasmas, respectively) best correspondence is with the curve 2 in the case of ohmic plasmas and with the curve 3 in the case of RF heating. The three chosen simulated spectra are shown in Figures 3 to 5 (lower).

For the two IW phases studied, the peripheral neutral densities are of the order of $4x10^{10}$ cm^{-3} and of $4x10^{11}$ cm^{-3}, respectively. These values seem larger than the corresponding values that would be inferred by a quantitative analysis of the D_α monitor signals. With the same assumptions as for the L phase, n_D-values of about 10^{10} cm^{-3} and of a few 10^{10} cm^{-3} would be deduced in front of the inner-wall for ohmic and RF-heated plasmas, respectively. Properly the Balmer α line analysis gives the n_D integrated line density. The situation in IW plasmas is different from that in L discharges in the respect that the last closed magnetic surface touches the inner-wall. Since the neutral energies and ionisation lengths are unknown, reliable quantitative comparison between the two techniques is difficult.

It has to be noted finally that the deduced "experimental" n_D-values are actually those existing at the C VI line emitting shells. Figure 8 in conjunction with Table 1 indicates the distance of these shells from the boundary. From Figure 7 it appears that at these shells the neutral density is about one order of magnitude less than at the limiter radius and in the SOL.

4.6 Qualitative considerations on the carbon ion brightness time evolution

The authenticity of the simulation can in principle be checked using absolute line radiances. Firstly, only the C IV and C III absolute line brightnesses are known, as previously mentioned in subsection 2.1. But they are not an indication of the volume "average" density of these

ions, since these particular ion influxes are localised in regions where there is plasma and solid material contact [10]. An estimation of the carbon content (carbon is the main impurity in the discharge studied) could be given by the Z_{eff}-values from visible bremsstrahlung emission. Its value is nearly constant at about 3. However, the presence of a few percent of ^3He (which is not measurable precisely in the discharge) prevents any accurate quantitative inference based on Z_{eff}.

Qualitatively, our analyses show it is impossible to simulate the constancy of C VI Lyα and Lyβ and of C V R at the L-IW transition without modifying the transport parameters. This is a consequence of the dependence of the C ion brightnesses on the neutral density n_D discussed in subsection 4.2. Physically an increase of the peaking of the carbon ion total density profile (ie. of the V_A/D_A ratio) after moving to the inner-wall would require less peripheral carbon ions to generate the same central carbon ion density. Such a reduction would compensate for the increase in brightnesses, that would otherwise result from the increased n_D dependence of brightnesses.

The relative constancy of Lyα with respect to Lyβ is correctly simulated, since their ratio is always of the order of 8.5-9. This figure is in agreement with the experimental ratio in cases when the pixel gain fatigue correction is negligible.

The relative variations of Balmer α with respect to Lyman α are in agreement with their relative time evolutions shown in Figure 2. The three "spectral best fitting" simulations give brightness ratios equal to 0.07, 0.12 and 0.17, respectively, on taking F(n) = 1 for both lines.

Experimental values for the G-ratio, with the "hole correction" included, are found to be equal to 0.45-0.50 for L-plasmas and to 0.65-0.7 for both IW plasmas. Again for the three "spectral best fitting" conditions, we find, respectively, 0.49, 0.74 and 0.77. We consider the agreement quite satisfactory, bearing in mind the experimental uncertainties, the inaccuracies of the atomic physics model and the fact that the G-ratio is an inverse function of T_e and therefore quite sensitive to errors in the peripheral T_e profile. It has, however, to be stressed that to simulate G-ratios larger than 0.60 in plasma regions with T_e larger than about 150-200 eV requires the CX population of the triplet level to be taken into account.

5. CONCLUSIONS

In hot JET deuterium plasmas, C VI emission arises from collision processes, which, in the absence of neutral hydrogen beam heating, occur near the plasma boundary. In comparison with the limiter discharges, distortions to the Lyman decrement (such as Lyβ/Lyγ and Lyβ/Lyδ ratios) and enhancements of the high series members (around 1s-12p) are observed after the plasma has been brought into contact with the carbon inner-wall.

The intensities of the Lyman spectrum members are interpreted in terms of low energy electron transfer from thermal D° atoms to C^{6+} ions as well as electron excitation of C^{5+} in their ground state.

The line of sight emission along the major torus radius is modelled using an impurity transport code which uses the experimental n_e and T_e radial profiles. The neutral deuterium density profile is introduced into the code by maintaining the central region values in the range given by NPA data analysis, whilst the peripheral values towards the limiter radius are adjusted to match the experimental results.

Electron transfer from excited states of D° (up to n = 5) as well as from the ground state have to be included to give satisfactory agreement with the Lyman spectra for ohmic and RF-heated plasmas. The cross sections for CX from the ground state are obtained from the CCMO model [27], whereas those for CX from excited states have been estimated using a simple universal Landau-Zener model. Comparison of relative intensities with model calculations allow plausible corrections F(n) to be made to the effective charge-exchange rate coefficients Q^{CX}_{n-1} as a function of the principal quantum number n of the upper level. For large n-values, F(n) is determined in such a way as to reproduce the experimental spectrum towards the series limit (including the observed "bump" around n = 12), whereas for n = 4,5 F(n) is chosen in such a way as to simulate the Lyβ/Lyγ and the Lyβ/Lyδ ratios. Taking F(4,5) = 1, it was not possible to simulate the smallest ratios experimentally (even on increasing $n_D(r)$ up

to a maximum reasonable limit based on NPA and D_α monitor data). The F(n)-values must also not be too large, to maintain consistency with the total CX cross-section, which is believed to be quite reliable. Moreover, for limiter plasmas, with well-defined scrape-off layers, the modelling of D_α monitor signals gives plausible values for the peripheral D° densities [~ 1.5-3 10^9 cm^{-3}] which are also correctly obtained by the Lyman spectrum simulations. On the other hand, for ohmic inner-wall and RF-heated inner-wall plasmas, the necessary peripheral D° densities for the simulations are one and two orders of magnitude higher, respectively. Comparison with the D_α signals from the inner-wall is prevented by the unknown D° ionisation length in front of the inner-wall.

The analysed data refer to the region r/a_L ~ 0.8, where the Lyman series emission shells are located. In this region the n_D-values are approximately one order of magnitude less than at the true periphery.

The observations offer a potential method of measuring local D° concentrations near the boundary of high temperature, high D° recycling plasmas. The method relies upon good peripheral $n_e(r)$ and $T_e(r)$ profiles around r/a_L ~ 0.7 - 0.9 and reliable extrapolation into the scrape-off layer. The present accuracy of this method of determining relative $n_D(r)$ from spectral features is to within an the order of magnitude at the plasma boundary. This is the difference between the peripheral values of the $n_D(r)$ curves shown in Figure 7 and used in the numerical simulations.

Difficulties were found in simulating the correct brightness time evolutions at the limiter to inner-wall shift. This is especially true for the almost constant intensity of the C VI and C V resonance lines. Results are inconclusive, but they do imply necessarily a change of the impurity total density profile, which must be more peaked for IW plasmas. On the other hand, the relative variations of both C VI Lyβ and Balmer α relative to C VI Lyα and the increased G-ratios after moving to inner-wall were satisfactorily simulated. For the latter the inclusion of CX recombination into the triplet levels is essential. Simulations of the less ionized species C IV and C III lines were not attempted, since their emission is localized in front of the inner-wall. The authors recognize that the one dimensional nature of the transport model may have some inadequacies in interpreting line emission which may exhibit poloidal asymmetries.

The F(n) corrections for n = 4,5 are of the order of the expected accuracy of the cross-section evaluations for charge-exchange from ground state D° atoms. By contrast, F(n) corrections for higher n are fairly large. The simple universal Landau-Zener model adopted as a starting point for the present study has no prior demonstration of reliability for capture from excited D° states. The general expectation is that it should give a lower limit for results and this appears to be confirmed here. Detailed studies in progress show that indeed the charge-exchange from excited states of deuterium at low energy is dominated by a small number of active curve-crossings and that a Landau-Zener approximation is a suitable starting point. However the accurate Landau-Zener parameters are significantly different from those adopted here. Also the crossing radii, corresponding to a given initial D° n-shell, vary significantly for the different molecular symmetries. It is anticipated that the more accurate calculations to be published will confirm the trend of multipliers F(n) indicated by the experiment here.

The region of $n \leq 15$ up to the series limit cannot be considered adequately treated in the present work. The analysis procedure has exploited the separability of excitation and change-exchange parts of the effective rate coefficients for photon emission. Also the deuterium collision limit has been introduced sharply into the calculations. In the continuation through the C^{5+} collision limit to the series limit and on into the free-bound continuum, clearly radiative recombination, three-body recombination and collisional-radiative processes between n-shells should enter the calculations. These refinement should not disturb the present conclusions covering the region $n \leq 15$.

ACKNOWLEDGMENTS

We would like to acknowledge the JET team for making possible this study, for technical support and for providing other diagnostic information. In particular, it is a pleasure to acknowledge discussions with Drs S. CORTI and P. MORGAN and their permission to use experimental data from the neutral particle analysers and from the D_α monitors. Thanks are due also to Dr B. SAOUTIC who developed the extension of the impurity ion transport code to large plasma sizes.

TABLE 1

Electron temperatures [keV] and electron densities [$10^{13}cm^{-3}$] adopted in the code for the simulation of the three experimental spectra shown in Figures 3 to 5 (upper). The values at the centre, at the radius a_c of maximum simulated C VI line emissivity (the simulated spectra being given in Figures 3 to 5 (lower)) and at the limiter radius a_L are given. All radii are in cm.

Plasma	Centre			Peak emission			Limiter		
	r=0	T_e	n_e	$r=a_c$	T_e	n_e	$r=a_L$	T_e	n_e
L	0	2.9	2.25	96	0.28	1.25	112	0.08	0.15
IW	0	2.9	2.45	96	0.30	1.35	118	0.075	0.22
RF-heated IW	0	4.4	3.4	98	0.60	2.2	120	0.15	0.25

TABLE 2

Multiplicative factors F(n) of the theoretical effective CX rate coefficients Q_{n-1}^{CX} used to obtain the four simulated spectra shown in Figure 9 in the case of IW plasmas and using curve 3 of Figure 7b for $n_D(r)$.

Spectrum	F(2,3)	F(4,5)	F(6-9)	F(10-15)
a	1	1	1	1
b	1	1	2.5	4.
c	1	1.5	2.5	4.
d	1	2.5	4.	7.

TABLE 3

The same as Table 2 for the spectra shown in Figure 10 in the case of L plasmas and using various $n_D(r)$ curves taken from Figure 7a.

Spectrum	n (r) curve	F(2,3)	F(4,5)	F(6-9)	F(10-15)
a	no neutrals	-	-	-	-
b	3	1	1.5	2.5	4.
c	4	1	1.5	2.5	4.
d	3	1	2.5	4.	7.

TABLE 4

Experimental and simulated Lyβ/Lyγ and Lyβ/Lyδ ratios for the three phases of the discharge studied. The "time" column gives the integration interval of the experimental spectra. Column "C" indicates the n_D curve number as given in Figure 7 (a for L plasmas, b for both IW plasmas). F(n) is the same as for spectra b in Tables 2 and 3.

DISCHARGE	TIME (sec)	EXPERIMENT		SIMULATION											
		β/γ	β/δ	C	β/γ	β/δ	C	β/γ	β/δ	C	β/γ	β/δ	C	β/γ	β/δ
L	2.5-4.2	2.75	6.6	No	3.1	6.8	1	3.0	6.7	2	2.9	6.6	3	2.65	6.4
IW	7.7-10.0	1.95	4.7	1	2.15	5.9	2	1.8	5.4	3	1.6	5.0	4	1.5	4.8
RF-heated IW	13.2-14.0	1.35	4.2	2	1.5	4.8	3	1.35	4.5	4	1.27	4.37	5	1.24	4.33

REFERENCES

[1] R.C. Isler, Phys. Scripta 35, 650 (1987)

[2] A. Boileau, M. Von Hellermann, L.D. Horton, J. Spence and H.P. Summers, JET Report JET-P(87)44 (1987)

[3] J.E. Rice, E.S. Marmar, J.L. Terry, E. Källne and J. Källne, Phys. Rev. Lett. 56, 50 (1986)

[4] J.E. Rice, E.S. Marmar, E. Källne and J. Källne, Phys. Rev. A 35, 3033 (1987)

[5] R.C. Isler and R.E. Olson, Phys. Rev. A 37, 3399 (1988)

[6] J.L. Schwob, A.W. Wouters, S. Suckewer and M. Finkenthal, Rev. Sci. Instrum. 58, 1601 (1987)

[7] R.J. Fonck, A.T. Ramsey and R.V. Yelle, Appl. Optics 21, 2115 (1982)

[8] H. Salzmann, K. Hirsch, P. Nielsen, C. Gowers, A. Godd, M. Gadeberg, H. Murmann and C. Schrödter, Nucl. Fusion 27, 1925 (1987)

[9] D. Veron, in Workshop on Diagnostics for Fusion Reactor Conditions (Varenna, September 1982), edited by Commission of European Communities, p 283 (1983)

[10] K.H. Behringer, B. Denne, M.J. Forrest, M.F. Stamp and H.P. Summers, presented at the 27th annual Meeting of the APS Division of Plasma Physics, San Diego, November 1985 (unpublished, but Poster Presentation available in JET Report JET-P(85)31)

[11] B. Saoutic, J. Ramette, M. Mattioli, B. Denne, K. Behringer, G. Magyar, N. Peacock, A. Ravestein, J.L. Schwob, F. Sieweke and A. Talbot, JET Report JET-R(87)14 (1987)

[12] K. Behringer, B. Denne, G. Magyar, M. Mattioli, N.J. Peacock, J. Ramette, B. Saoutic and J.L. Schwob, Journal de Physique, Colloque C1, Supplément au n° 3, 49, C1-387 (1988)

[13] J.G. Timothy, Rev. Sci. Instrum. 52, 1131 (1981)

[14] TFR Group, Nucl. Fusion 25, 981 (1985)

[15] K. Lackner, K. Behringer, W. Engelhardt and R. Wunderlich, Z. Naturforsch. 37a, 931 (1982)

[16] K.L. Bell, H.B. Gilbody, J.G. Hughes, A.E. Kingston and F.J. Smith, J. Phys. Chem. Ref. Data 12, 891 (1983)

[17] M.A. Lennon, K.L. Bell, H.B. Gilbody, J.G. Hughes, A.E. Kingston, M.J. Murray and F.J. Smith, J. Phys. Chem. Ref. Data 17, 1285 (1988)

[18] M. Mattioli, Cadarache Laboratory Report EUR-CEA-FC 1346 (1988)

[19] "Atomic Data for Fusion, Vol. 5" (R.A. Phaneuf, R.K. Janev and M.S. Pindzola eds.), ORNL Report ORNL-6090/V5 (1987)

[20] R.E.H. Clark, N.H. Magee, J.B. Mann Jr. and A.L. Merts, Astrophys. J. 254, 412 (1982)

[21] D.M. Cochrane and R.W.P. McWhirter Phys. Scripta 28, 25 (1983)

[22] S.S. Tayal and A.E. Kingston, J. Phys. B : At. Mol. Phys. 17, L145 (1984)

[23] S.S. Tayal, Phys. Rev. A 34, 1847 (1986)

[24] TFR Group, J.G. Doyle and J.L. Schwob, J. Phys. B : At. Mol. Phys. 15, 813 (1982)

[25] R. Mewe and J. Schrijver, Astron. Astrophys. 65, 99 (1978)

[26] J. Spence and H.P. Summers, J. Phys. B : At. Mol. Phys. 19, 3749 (1986)

[27] T.A. Green, E.J. Shipsey, J.C. Browne, Phys. Rev. A 25, 1364 (1982)

[28] R.E. Olson and A. Salop, Phys. Rev. A 14, 579 (1976)

[29] R. Mann, F. Folkmann and H.F. Beyer, J. Phys. B : At. Mol. Phys. 14, 1161 (1981)

[30] S. Corti, G. Bracco, M. Brusati, A. Gondhalekar, G. Grosso, F. Hendriks, S. Segre and V. Zanza, in 12th European Conference on Plasma Fusion, Budapest September 1985, Europhysics Abstracts Vol. 9F (L Pocs and A. Montvai eds.) Vol I, p 219 (1985)

[31] K.H. Behringer, P.G. Carolan, B. Denne, G. Decker, W. Engelhardt et al., Nucl. Fusion 26, 751 (1986)

[32] K. Behringer, A. Boileau, F. Bombarda, B. Denne, W. Engelhardt et al., in "Plasma Physics and Controlled Nuclear Fusion Research" (Proc. 11th Conference, Kyoto 1986) 1, 197 (IAEA, Vienna, 1987)

[33] L.C. Johnson and E. Hinnov, J. Quant. Spectrosc. Radiat. Transfer 13, 333 (1973)

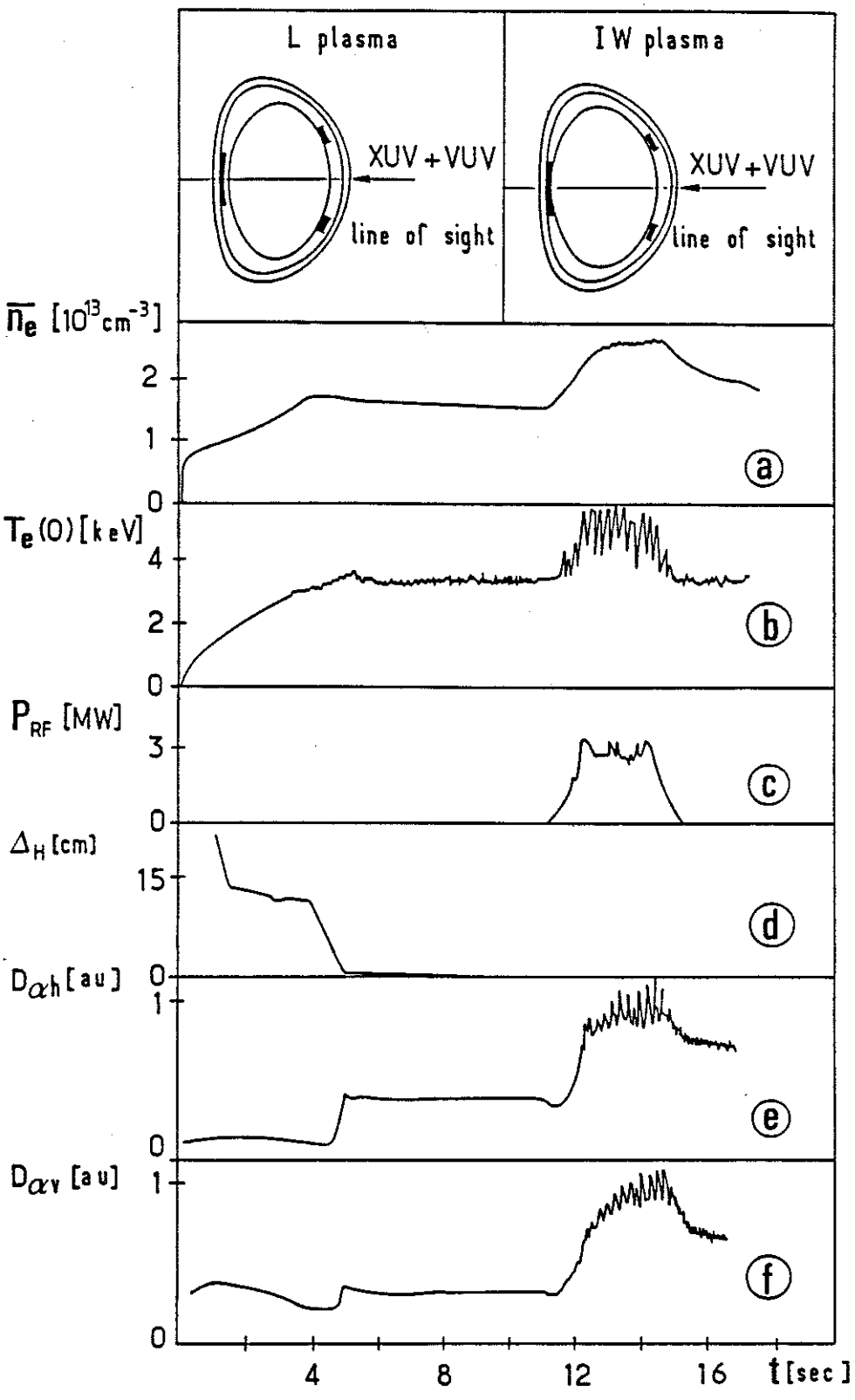

Fig. 1 Time evolution of a few signals for JET discharge #13751: (a) line-integrated average electron density $\bar{n}_e$ along a vertical chord through the plasma centre, (b) central electron temperature $T_e(0)$, (c) RF power P_{RF}, (d) plasma horizontal displacement Δ_H of the plasma border from the inner-wall, (e) D_α monitor signal viewing the inner-wall horizontally $D_{\alpha h}$, (f) vertical D_α monitor signal $D_{\alpha v}$. Top insets: schematic of the position of the last closed magnetic surface with respect to the inner-wall and to the two outer belt limiters for L plasma (left) and IW plasmas (right).

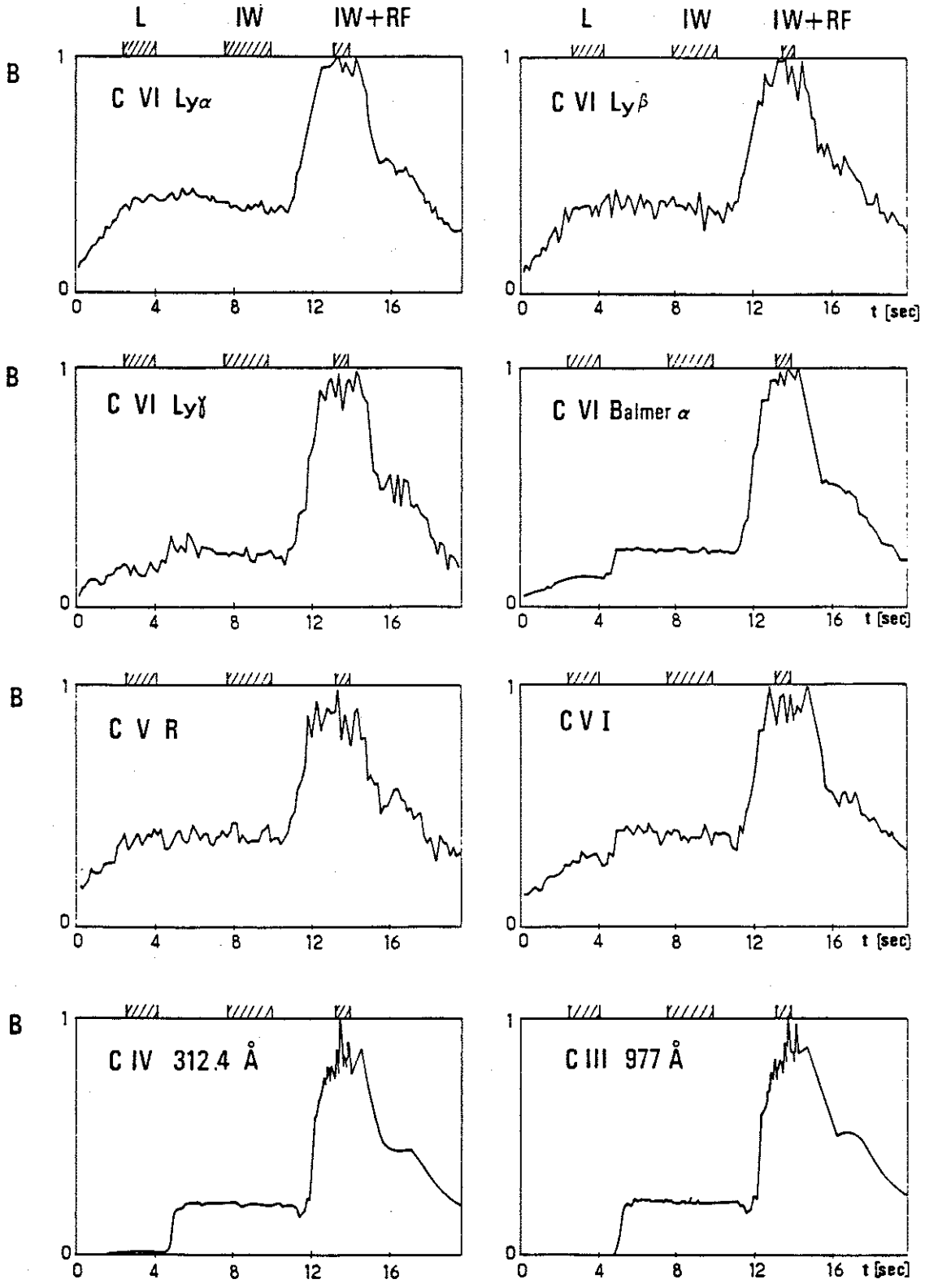

Fig. 2 Time evolution of the brightnesses B of the following carbon lines: C VI Lyman α, β and γ, C VI Balmer α, C V R and I, CIV 312.4 Å and C III 977 Å. The three hatched time intervals correspond to the times over which the Lyman series spectra shown in Fig. 3 to 5 were averaged.

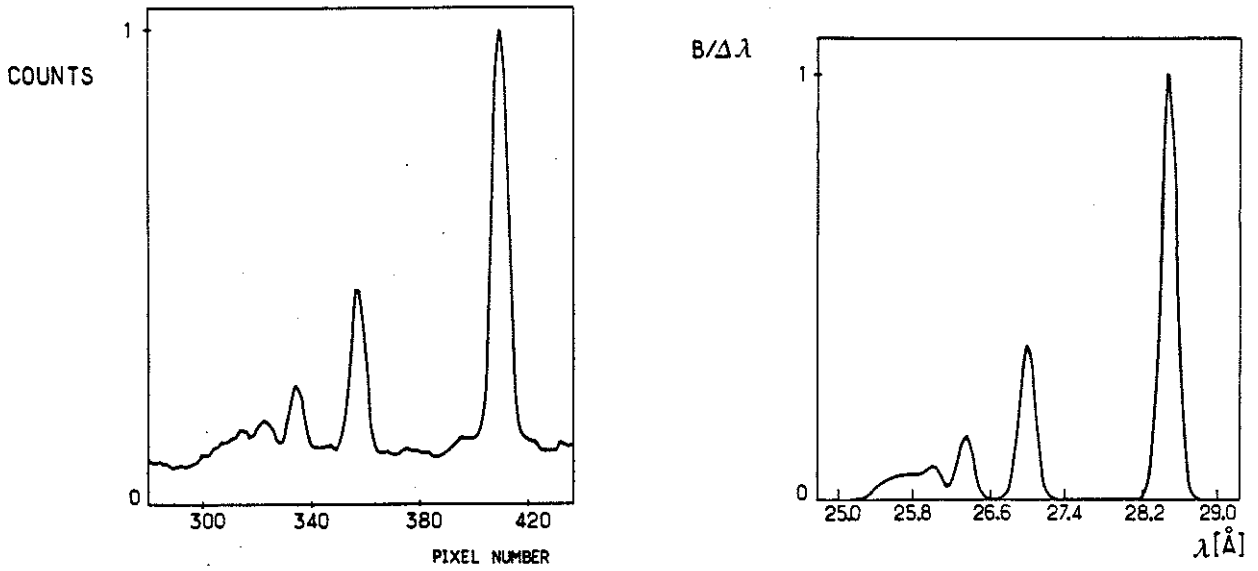

Fig. 3 Left: experimental L plasma Lyman series spectrum integrated between 2.5 and 4.2 sec., the count number C, normalized to its maximum value at the Lyman β wavelength, is given as function of the pixel number. Right: simulated spectrum using the dotted curve of Fig. 7a for $n_D(r)$. The calculated brightness per unit wavelength $B/\Delta\lambda$ is plotted as function of the wavelength. The normalisation is the same as for the left figure.

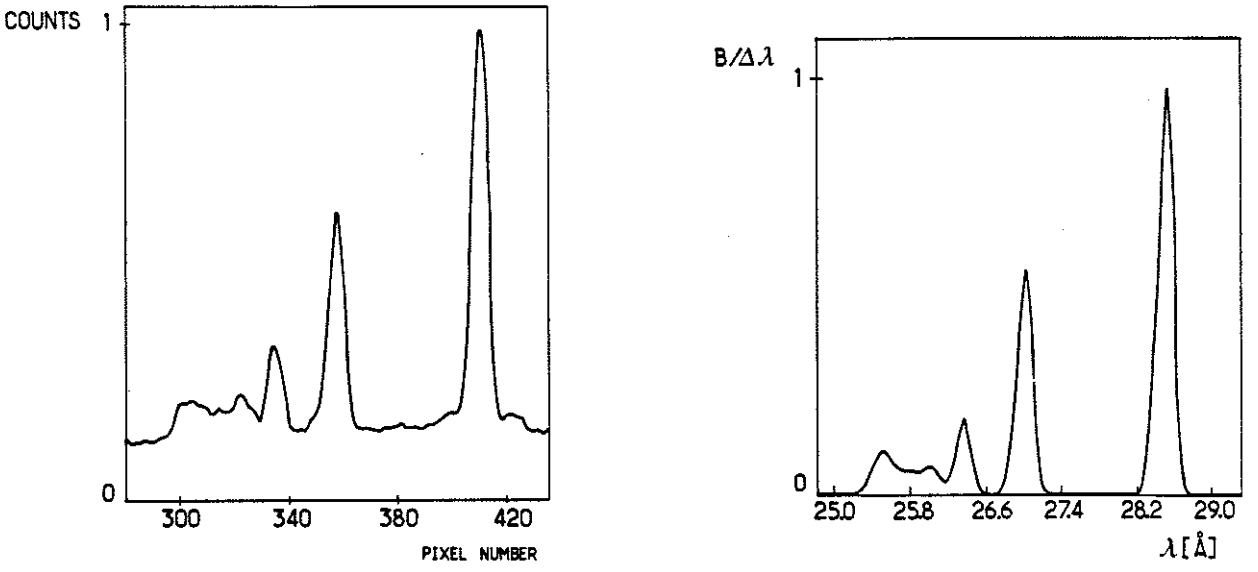

Fig. 4 The same as Fig. 3 for ohmic IW plasmas with the experimental spectrum integrated between 7.7 and 10.0 sec. The simulated spectrum is obtained using curve 2 of Fig. 7b for $n_D(r)$.

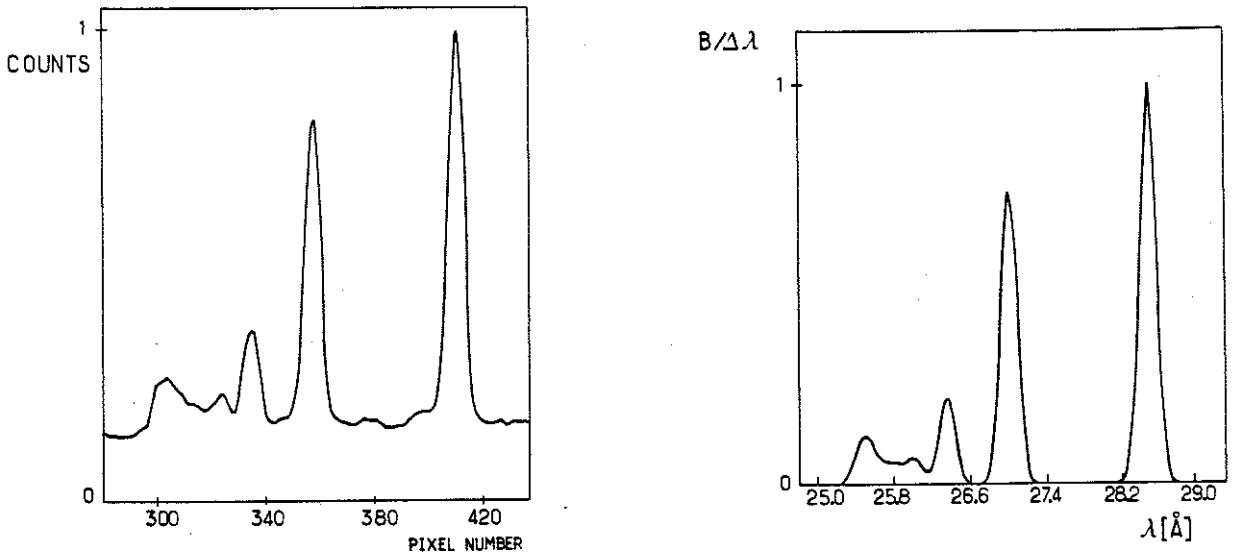

Fig. 5 The same as Fig. 3 for RF-heated IW plasmas with the experimental spectrum integrated between 13.2 and 14.0sec. The simulated spectrum is obtained using curve 3 of Fig. 7b for $n_D(r)$.

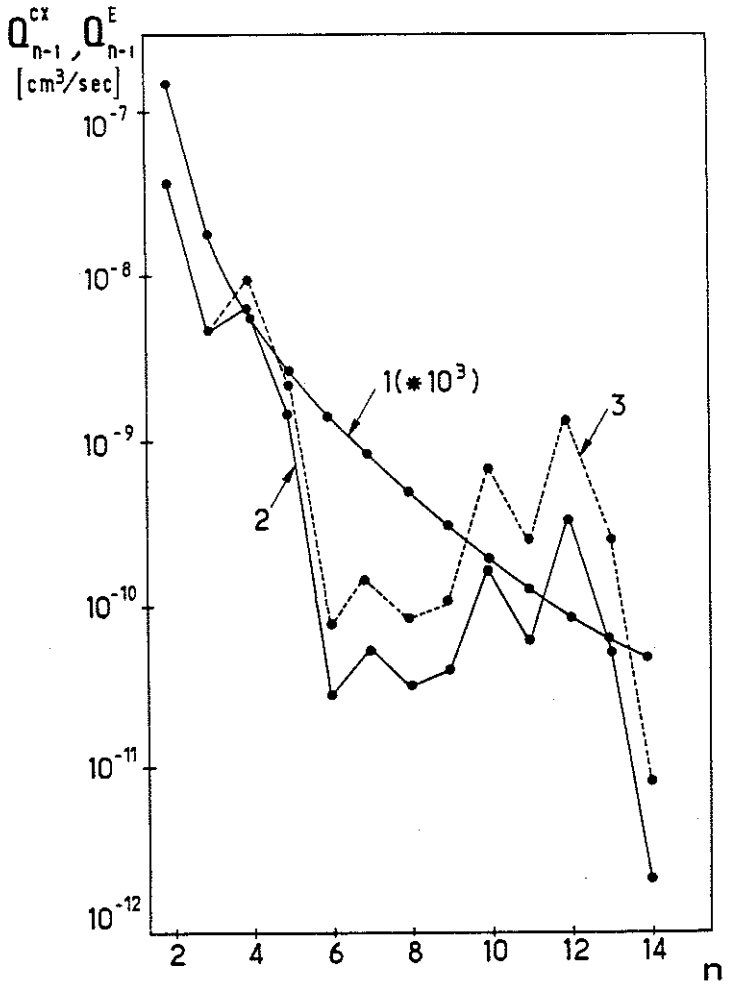

Fig. 6 Effective excitation rate coefficients for photon emission of Lyman series lines as a function of the principal quantum number n of the upper level. Curve 1 (solid): rate coefficients for electron impact from ground state Q^{E}_{n-1} (*10^3), curve 2 (solid): rate coefficients for charge-exchange with deuterium atoms Q^{CX}_{n-1}, curve 3 (dashed): 'corrected' rates $F(n)\,Q^{CX}_{n-1}$, after multiplication by an n-dependent multiplicative factor $F(n)$ ($F(4,5)=1.5$, $F(6\text{-}9)=2.5$, $F(10\text{-}14)=4$). The rates shown are calculated for plasma parameters close to the region of maximum C VI line emission as follows: $n_e=1.4$ $10^{13}\,\mathrm{cm}^{-3}$, $T_e\sim 500\,\mathrm{eV}$, $T_i=T_D=T_e$, $Z_{eff}=2$).

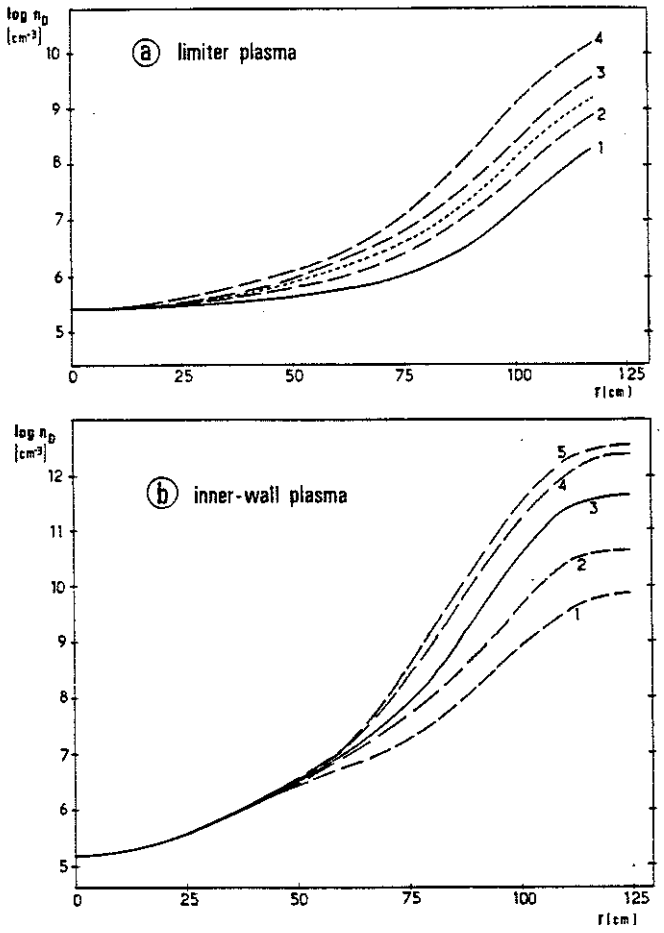

Fig. 7 Logarithm of the thermal neutral deuterium density profiles $n_D(r)$ adopted in the impurity transport simulation code. (a): L plasmas, (b): IW plasmas. The solid curves show the initial profiles, suggested by NPA data. The dashed curves show the other profiles used for the simulations. The dotted line in (a) shows the n_D profile which gives the best agreement for L plasmas. The limiter radii a_L are given in Table 1, the last mesh radii a are about 5 cm larger than a_L.

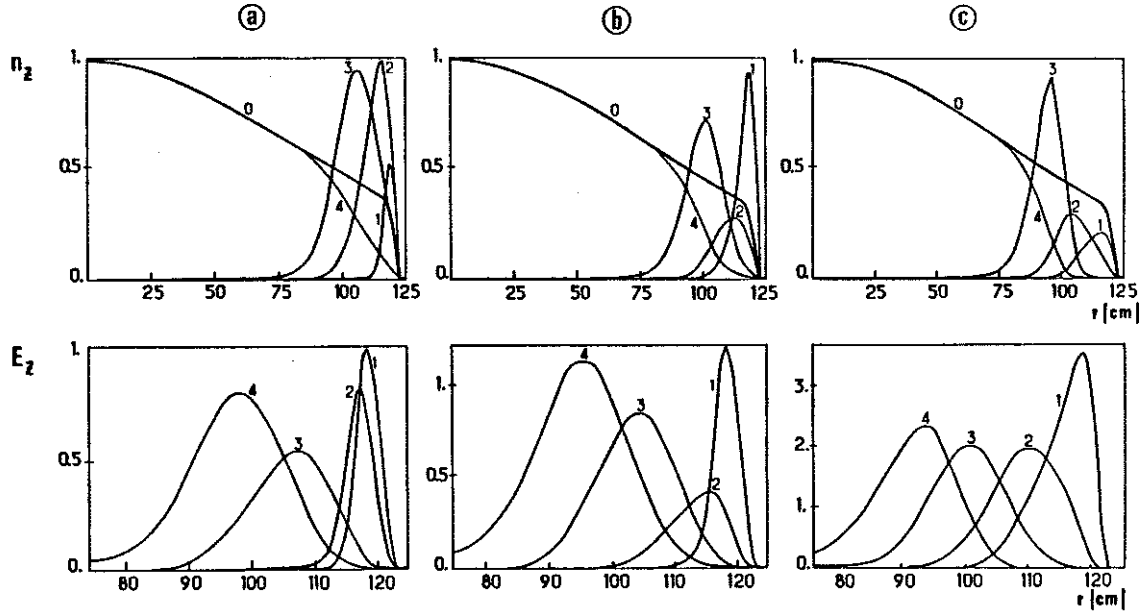

Fig. 8 Simulated ion radial density profiles $n_Z(r)$ (upper) and simulated emissivity radial profiles $E_Z(r)$ (lower): (from left to right) (a) without neutrals, (b) with n_D(r) from curve 2 of Fig. 7b, (c) with $n_D(r)$ from curve 3 of Fig. 7b. Steady state solution for IW plasmas, $D_A = 10000\,\mathrm{cm}^2/\mathrm{sec}$, $V_A = 200\,\mathrm{cm/s}$.

Legend of the upper curves including (right) the scale multiplicative factors for cases (a), (b) and (c), respectively:

(0) : total ion density ; 1, 1, 1
(1) : Li-like ions ; 10, 10, 1
(2) : He-like ions ; 5, 1, 1
(3) : H-like ions ; 10, 5, 5
(4) : fully stripped ions ; 1, 1, 1

Legend of the lower curves including (right) the scale multiplicative factors for cases (a), (b) and (c), respectively:

(1) : CIII 977 Å ; 1, 1, 1
(2) : CIV 312.4 Å ; 5, 1, 1
(3) : CV R ; 10, 5, 5
(4) : CVI Ly β ; 100, 50, 50

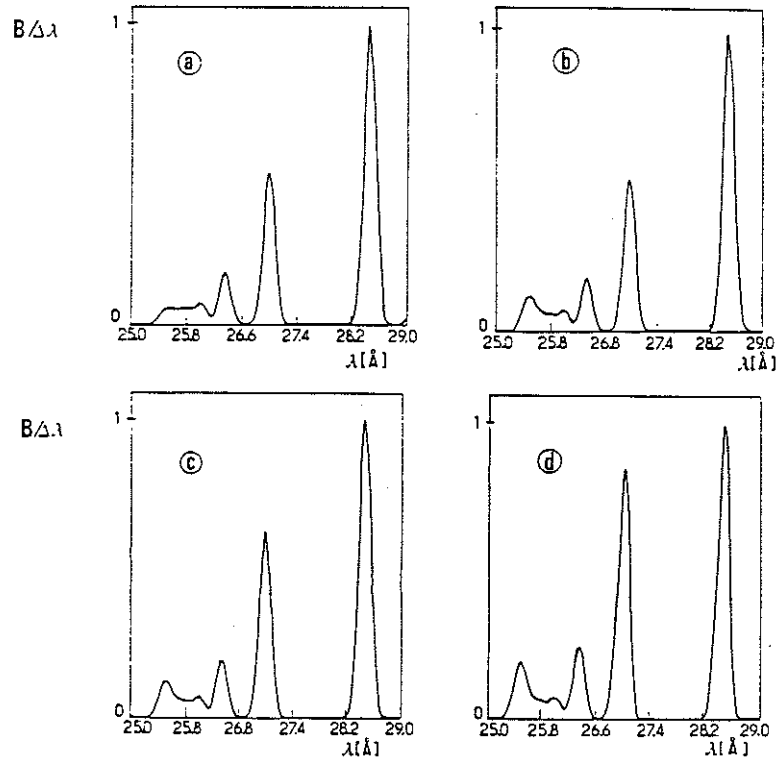

Fig. 9 Simulated spectra for IW plasmas $B/\Delta\lambda$ (same as Fig. 3 lower) using curve 3 of Fig. 7b for n_D and with $F(n)$ multiplicative factors are given in Table 2.

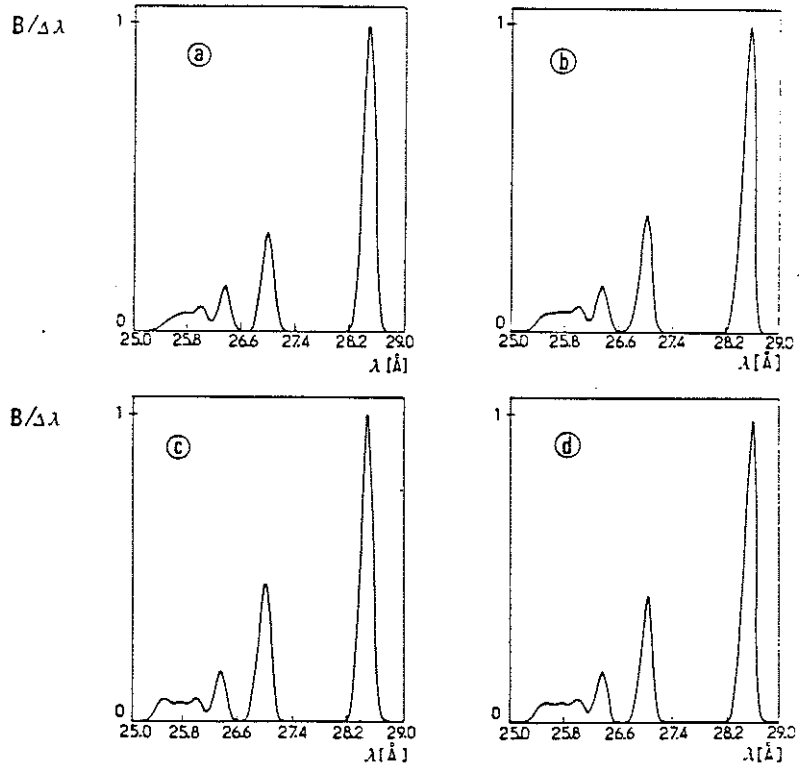

Fig. 10 Simulated spectra for L plasmas $B/\Delta\lambda$ (same as Fig. 3 lower), with n_D curves and $F(n)$ multiplicative factors as given in Table 3.

APPENDIX 1.

THE JET TEAM

JET Joint Undertaking, Abingdon, Oxon, OX14 3EA, U.K.

J.M.Adams[1], F.Alladio[4], H.Altmann, R.J.Anderson, G.Appruzzese, W.Bailey, B.Balet, D.V.Bartlett, L.R.Baylor[24], K.Behringer, A.C.Bell, P.Bertoldi, E.Bertolini, V.Bhatnagar, R.J.Bickerton, A.Boileau[3], T.Bonicelli, S.J.Booth, G.Bosia, M.Botman, D.Boyd[31], H.Brelen, H.Brinkschulte, M.Brusati, T.Budd, M.Bures, T.Businaro[4], H.Buttgereit, D.Cacaut, C.Caldwell-Nichols, D.J.Campbell, P.Card, J.Carwardine, G.Celentano, P.Chabert[27], C.D.Challis, A.Cheetham, J.Christiansen, C.Christodoulopoulos, P.Chuilon, R.Claesen, S.Clement[30], J.P.Coad, P.Colestock[6], S.Conroy[13], M.Cooke, S.Cooper, J.G.Cordey, W.Core, S.Corti, A.E.Costley, G.Cottrell, M.Cox[7], P.Cripwell[13], F.Crisanti[4], D.Cross, H.de Blank[16], J.de Haas[16], L.de Kock, E.Deksnis, G.B.Denne, G.Deschamps, G.Devillars, K.J.Dietz, J.Dobbing, S.E.Dorling, P.G.Doyle, D.F.Düchs, H.Duquenoy, A.Edwards, J.Ehrenberg[14], T.Elevant[12], W.Engelhardt, S.K.Erents[7], L.G.Eriksonn[5], M.Evrard[2], H.Falter, D.Flory, M.Forrest[7], C.Froger, K.Fullard, M.Gadeberg[11], A.Galetsas, R.Galvao[8], A.Gibson, R.D.Gill, A.Gondhalekar, C.Gordon, G.Gorini, C.Gormezano, N.A.Gottardi, C.Gowers, B.J.Green, F.S.Griph, M.Gryzinski[26], R.Haange, G.Hammett[6], W.Han[9], C.J.Hancock, P.J.Harbour, N.C.Hawkes[7], P.Haynes[7], T.Hellsten, J.L.Hemmerich, R.Hemsworth, R.F.Herzog, K.Hirsch[14], J.Hoekzema, W.A.Houlberg[24], J.How, M.Huart, A.Hubbard, T.P.Hughes[32], M.Hugon, M.Huguet, J.Jacquinot, O.N.Jarvis, T.C.Jernigan[24], E.Joffrin, E.M.Jones, L.P.D.F.Jones, T.T.C.Jones, J.Källne, A.Kaye, B.E.Keen, M.Keilhacker, G.J.Kelly, A.Khare[15], S.Knowlton, A.Konstantellos, M.Kovanen[21], P.Kupschus, P.Lallia, J.R.Last, L.Lauro-Taroni, M.Laux[33], K.Lawson[7], E.Lazzaro, M.Lennholm, X.Litaudon, P.Lomas, M.Lorentz-Gottardi[2], C.Lowry, G.Magyar, D.Maisonnier, M.Malacarne, V.Marchese, P.Massmann, L.McCarthy[28], G.McCracken[7], P.Mendonca, P.Meriguet, P.Micozzi[4], S.F.Mills, P.Millward, S.L.Milora[24], A.Moissonnier, P.L.Mondino, D.Moreau[17], P.Morgan, H.Morsi[14], G.Murphy, M.F.Nave, M.Newman, L.Nickesson, P.Nielsen, P.Noll, W.Obert, D.O'Brien, J.O'Rourke, M.G.Pacco-Düchs, M.Pain, S.Papastergiou, D.Pasini[20], M.Paume[27], N.Peacock[7], D.Pearson[13], F.Pegoraro, M.Pick, S.Pitcher[7], J.Plancoulaine, J-P.Poffé, F.Porcelli, R.Prentice, T.Raimondi, J.Ramette[17], J.M.Rax[27], C.Raymond, P-H.Rebut, J.Removille, F.Rimini, D.Robinson[7], A.Rolfe, R.T.Ross, L.Rossi, G.Rupprecht[14], R.Rushton, P.Rutter, H.C.Sack, G.Sadler, N.Salmon[13], H.Salzmann[14], A.Santagiustina, D.Schissel[25], P.H.Schild, M.Schmid, G.Schmidt[6], R.L.Shaw, A.Sibley, R.Simonini, J.Sips[16], P.Smeulders, J.Snipes, S.Sommers, L.Sonnerup, K.Sonnenberg, M.Stamp, P.Stangeby[19], D.Start, C.A.Steed, D.Stork, P.E.Stott, T.E.Stringer, D.Stubberfield, T.Sugie[18], D.Summers, H.Summers[20], J.Taboda-Duarte[22], J.Tagle[30], H.Tamnen, A.Tanga, A.Taroni, C.Tebaldi[23], A.Tesini, P.R.Thomas, E.Thompson, K.Thomsen[11], P.Trevalion, M.Tschudin, B.Tubbing, K.Uchino[29], E.Usselmann, H.van der Beken, M.von Hellermann, T.Wade, C.Walker, B.A.Wallander, M.Walravens, K.Walter, D.Ward, M.L.Watkins, J.Wesson, D.H.Wheeler, J.Wilks, U.Willen[12], D.Wilson, T.Winkel, C.Woodward, M.Wykes, I.D.Young, L.Zannelli, M.Zarnstorff[6], D.Zasche[14], J.W.Zwart.

PERMANENT ADDRESS

1. UKAEA, Harwell, Oxon. UK.
2. EUR-EB Association, LPP-ERM/KMS, B-1040 Brussels, Belgium.
3. Institute National des Récherches Scientifique, Quebec, Canada.
4. ENEA-CENTRO Di Frascati, I-00044 Frascati, Roma, Italy.
5. Chalmers University of Technology, Göteborg, Sweden.
6. Princeton Plasma Physics Laboratory, New Jersey, USA.
7. UKAEA Culham Laboratory, Abingdon, Oxon. UK.
8. Plasma Physics Laboratory, Space Research Institute, Sao José dos Campos, Brazil.
9. Institute of Mathematics, University of Oxford, UK.
10. CRPP/EPFL, 21 Avenue des Bains, CH-1007 Lausanne, Switzerland.
11. Risø National Laboratory, DK-4000 Roskilde, Denmark.
12. Swedish Energy Research Commission, S-10072 Stockholm, Sweden.
13. Imperial College of Science and Technology, University of London, UK.
14. Max Planck Institut für Plasmaphysik, D-8046 Garching bei München, FRG.
15. Institute for Plasma Research, Gandhinagar Bhat Gujat, India.
16. FOM Instituut voor Plasmafysica, 3430 Be Nieuwegein, The Netherlands.
17. Commissiariat à L'Energie Atomique, F-92260 Fontenay-aux-Roses, France.
18. JAERI, Tokai Research Establishment, Tokai-Mura, Naka-Gun, Japan.
19. Institute for Aerospace Studies, University of Toronto, Downsview, Ontario, Canada.
20. University of Strathclyde, Glasgow, G4 ONG, U.K.
21. Nuclear Engineering Laboratory, Lapeenranta University, Finland.
22. JNICT, Lisboa, Portugal.
23. Department of Mathematics, Univeristy of Bologna, Italy.
24. Oak Ridge National Laboratory, Oak Ridge, Tenn., USA.
25. G.A. Technologies, San Diego, California, USA.
26. Institute for Nuclear Studies, Swierk, Poland.
27. Commissiariat à l'Energie Atomique, Cadarache, France.
28. School of Physical Sciences, Flinders University of South Australia, South Australia SO42.
29. Kyushi University, Kasagu Fukuoka, Japan.
30. Centro de Investigaciones Energeticas Medioambientales y Techalogicas, Spain.
31. University of Maryland, College Park, Maryland, USA.
32. University of Essex, Colchester, UK.
33. Akademie de Wissenschaften, Berlin, DDR.

CR 88.49.1A